

Protocol for certifying entanglement in surface spin systems using a scanning tunneling microscope

Broekhoven, Rik; Lee, Curie; Phark, Soo Hyon; Otte, Sander; Wolf, Christoph

DOI

[10.1038/s41534-024-00888-9](https://doi.org/10.1038/s41534-024-00888-9)

Publication date

2024

Document Version

Final published version

Published in

NPJ Quantum Information

Citation (APA)

Broekhoven, R., Lee, C., Phark, S. H., Otte, S., & Wolf, C. (2024). Protocol for certifying entanglement in surface spin systems using a scanning tunneling microscope. *NPJ Quantum Information*, 10(1), Article 92. <https://doi.org/10.1038/s41534-024-00888-9>

Important note

To cite this publication, please use the final published version (if applicable). Please check the document version above.

Copyright

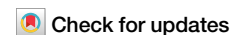
Other than for strictly personal use, it is not permitted to download, forward or distribute the text or part of it, without the consent of the author(s) and/or copyright holder(s), unless the work is under an open content license such as Creative Commons.

Takedown policy

Please contact us and provide details if you believe this document breaches copyrights. We will remove access to the work immediately and investigate your claim.



Protocol for certifying entanglement in surface spin systems using a scanning tunneling microscope



Rik Broekhoven¹, Curie Lee^{2,3}, Soo-hyon Phark^{2,4}, Sander Otte¹ & Christoph Wolf^{2,4}✉

Certifying quantum entanglement is a critical step toward realizing quantum-coherent applications. In this work, we show that entanglement of spins can be unambiguously evidenced in a scanning tunneling microscope with electron spin resonance by exploiting the fact that entangled states undergo a free time evolution with a distinct characteristic time constant that clearly distinguishes it from the time evolution of non-entangled states. By implementing a phase control scheme, the phase of this time evolution can be mapped back onto the population of one entangled spin, which can then be read out reliably using a weakly coupled sensor spin in the junction of the scanning tunneling microscope. We demonstrate through open quantum system simulations with currently available spin coherence times of $T_2 \approx 300$ ns, that a signal directly correlated with the degree of entanglement can be measured at temperatures of 100–400 mK accessible in sub-Kelvin scanning tunneling microscopes.

Recent advances in quantum control of surface spin systems have shown that this platform can be used to design quantum-coherent systems by tailoring the interaction of individual spins using the scanning tunneling microscope (STM) and atom manipulation^{1,2}. In such a system, quantum coherent control of single and multiple spins has been achieved by electron spin resonance (ESR), which is facilitated by resonant electric fields in the STM^{3–8}. When combining the atomic manipulation aspect and quantum coherent control, one can envision that this platform can be used to implement a reconfigurable quantum simulator in hardware using only a few atoms and an ESR-STM. By utilizing up to three titanium (Ti) atomic spins, some of us have demonstrated fundamental quantum gate operations such as controlled-NOT (CNOT) and controlled-controlled-NOT (CCNOT) gates on two layers of magnesium oxide (MgO)⁹. The next logical step is to certify entanglement in this atomic qubit platform, which is a strong prerequisite for studying quantum-coherent phenomena beyond individual quantum gate operations^{10,11}. This, however, is not straightforward in the ESR-STM since it only allows for time-averaged single spin read-out with long measurement times (ms or kHz)¹², compared to the typical time-scale for coherence time (T_2) of only several hundred nanoseconds^{4,13}. Previous works¹⁴ have suggested to use the magnetic susceptibility as entanglement witness; however, no experimental realization of this idea has yet been shown. Alternatively, one could exploit the fact that states that are not eigenstates of the system undergo a time evolution that can be probed by the time-averaging measurement of the STM as previously shown for the free time-evolution of spins initialized by bias voltage pulses in a system

tuned to singlet-triplet eigenstates¹⁵. In a similar manner one can use radio-frequency (RF) pulses in an ESR-STM to create entangled states that are no longer eigenstates in the Zeeman basis of the constituent spins, and therefore will undergo a time evolution that is distinctively different from the evolution of non-entangled states. This approach, also called phase reversal tomography¹⁶, has been previously applied to phosphorous donor semiconductor qubits¹⁷. Here, we present how to adapt and optimize this method for ESR-STM, which relies on the fact that ESR-STM has highly sensitive population read-out⁶. By using open quantum systems simulations and parameters compatible with typical experiments, we demonstrate that surface spins can be entangled with high fidelity at sufficiently low temperatures.

Results

Creating and measuring entanglement

It has been established that ESR-STM provides a universal gate set based on single-spin (or qubit) phase control¹⁸ and controlled-NOT gates⁹. In the following, we will discuss how to create entanglement in a surface spin system and subsequently measure it. We start from two weakly interacting spins, which can be realized in the experiment by using two Ti atoms^{2,6}. We require that the interaction between these spins is sufficiently weak so that their combined eigenstates can be written in good approximation as Zeeman product states, e.g. $|\uparrow\rangle_A \otimes |\uparrow\rangle_B = |\uparrow\uparrow\rangle$, where \uparrow (\downarrow) denotes the ground (excited) state of each spin, the subscripts A, B label the two spins, and \otimes denotes the tensor product. As shown in Fig. 1a, two spins $|\uparrow\uparrow\rangle$ can

¹Department of Quantum Nanoscience, Kavli Institute of Nanoscience, Delft University of Technology, 2628 CJ Delft, the Netherlands. ²Center for Quantum Nanoscience, Institute for Basic Science (IBS), Seoul, 03760, Korea. ³Department of Physics, Ewha Womans University, Seoul, 03760, Korea. ⁴Ewha Womans University, Seoul, 03760, Korea. ✉e-mail: wolf.christoph@qns.science

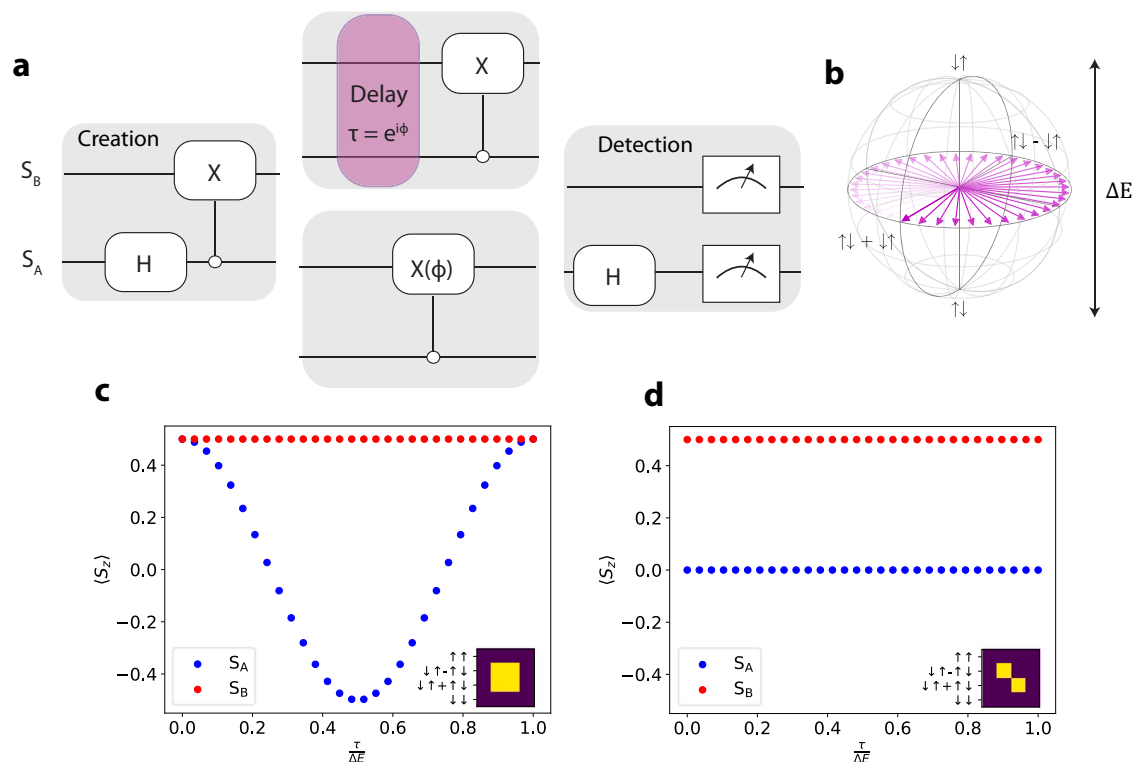


Fig. 1 | Sequence of quantum logic gates to demonstrate entanglement in ESR-STM. **a** shows the pulse scheme using a quantum gate notation. From left to right this scheme applies a Hadamard gate to spin A, a negative CNOT gate, a pulse delay (or phase-sweep) gate, and a disentangling gate scheme. Finally, both states can be

measured to determine their respective populations. **b** Bloch sphere shows the time-evolution of the entangled state on the equator. **c** Expected measurement signal for spin A and spin B when entangled and, in contrast, **(d)** the same measurement for two spins that are not entangled as emphasized by the density matrix in the inset.

be entangled by a Hadamard gate H followed by a negative controlled-NOT gate (CNOT= $|\uparrow\rangle\langle\uparrow| \otimes \mathbb{1} + |\downarrow\rangle\langle\downarrow| \otimes \sigma_x$), resulting in an entangled state $|\uparrow\downarrow\rangle + |\downarrow\uparrow\rangle$. In order to detect this entanglement, we can now exploit the fact that the entangled state is not an eigenstate of the Zeeman product basis and thus undergoes a free evolution¹⁵. During this evolution the state picks up a phase at a rate that is proportional to the energy splitting between $|\uparrow\downarrow\rangle$ and $|\downarrow\uparrow\rangle$ (Fig. 1b). The accumulated phase is distinct from the free evolution of any other non-entangled state and thus allows to uniquely witness the state as entangled. In particular, states that are maximally correlated but not entangled have no accumulated phase. We can measure the phase through a Bell state disentanglement measurement, realized by a CNOT followed by a Hadamard, which projects the phase onto one of the two spins followed by read-out of that spin. To be more precise the $|\uparrow\downarrow\rangle + |\downarrow\uparrow\rangle$ is projected upon $|\uparrow\downarrow\rangle$ whereas $|\uparrow\downarrow\rangle - |\downarrow\uparrow\rangle$, which has a phase of π , is projected upon $|\uparrow\uparrow\rangle$. The full protocol is illustrated in Fig. 1a. By repeating the scheme with increasing delay times between the entanglement and disentanglement sequences we can probe the full phase accumulation during free evolution. For the maximally entangled state it shows up as a slow (relative to the Larmor frequencies of the individual spins) variation of $\langle S_z \rangle$ as shown in Fig. 1c obtained from an analytical solution of the 4×4 density matrix shown in the inset. This variation can be read-out through the sensor-spin, where $\langle S_z \rangle \propto \Delta I^{ESR}$, i.e. the change in the tunneling current at spin resonance in the ESR-STM experiment⁶. In contrast, the maximally correlated state will result in a flat signal (Fig. 1d). To directly and unambiguously evidence entanglement, one has to ensure that the measurement shows an oscillation of spin A whereas spin B stays constant. In a practical implementation, probing free evolution might be slightly disadvantageous when the evolution time is either very short and approaches the typical rise and fall times of the signal generator, or very long and rivals the coherence times T_2 . Fortunately, the effect of free evolution can also be captured by

adjusting the phase ϕ on the second CNOT gate $X(\phi)$ such that $\phi = \tau/\Delta E$. In the following, we will use such as phase-sweep instead of a delay-time sweep.

Implementation

We will now discuss some details of the implementation. All simulations were carried out using the QuTiP package in the Lindblad formalism using collapse operators parameterized by T_1 and T_ϕ for energy relaxation and pure dephasing of each spin, respectively (see Methods)¹⁹. The total system consists of three spin 1/2 (labeled A, B, and R in Fig. 2a), which are exchanged coupled to one another sufficiently weakly so that the state diagram can be written to a good approximation as Zeeman product states (details of the system can be found in the methods section). We emphasize that only spins A and B will be the target of this entanglement scheme while spin R acts as sensor for the read-out. The Fe atoms are added in the experiment to provide the local field gradients for driving ESR of the remote spins (A and B)^{6,9}.

To achieve the desired gate sequence for entanglement, we first combine two rotations (labeled as $X_{\frac{\pi}{2}}, Y_\pi$, where X and Y denote the rotation axes and the subscript specifies the rotation angle) to perform a Hadamard gate and then a single-frequency pulse X_π to perform a CNOT (Fig. 2b). Note that in general in this system a single driving frequency always performs a conditional operation while an unconditional NOT gate requires multi-frequency driving⁹. We found that at low enough temperatures single-frequency driving can be used for all gates due to negligible population in the excited states (Fig. 2b). This no longer holds true at elevated temperatures, where excited states can have non-negligible populations. In such a case, the Hadamard gate results in an admixture of entangled states reflecting the excited state population. To avoid this, we also use single frequency driving for the Hadamard gate, which ensures that only the targeted fraction of population will be entangled, at the loss of overall signal amplitude. We have

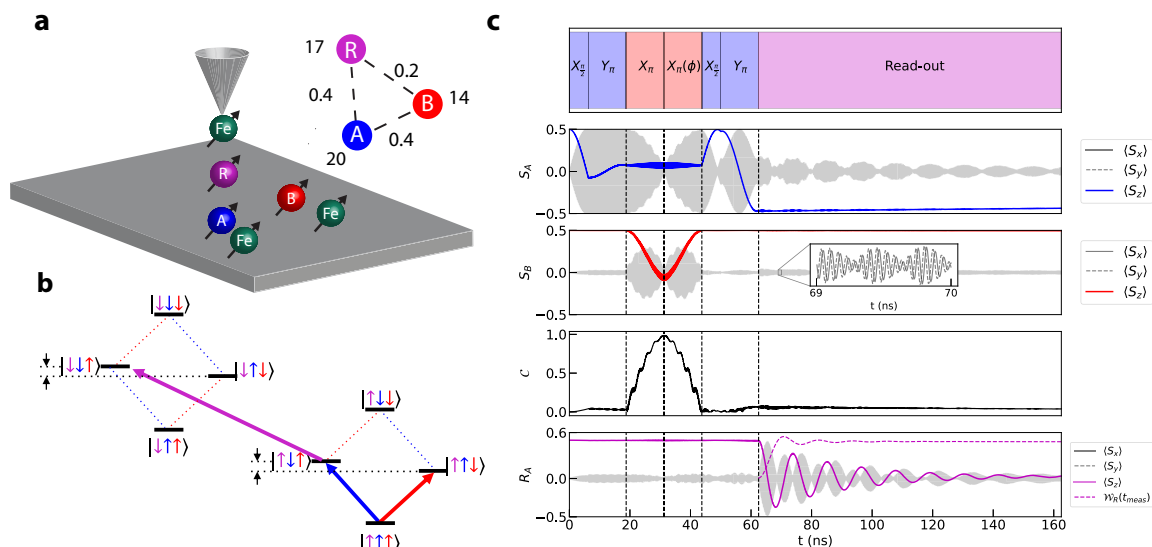


Fig. 2 | Two-spin entanglement scheme using sensor spin read-out. **a** Two relatively long-lived spins (A, B) are entangled while a third, short-lived sensor spin (R) is used for the read-out. Each pair of titanium and iron (Fe) atom serves as a qubit in the ESR-STM experiment. **b** Energy level diagram showing CNOT (red), Hadamard (blue) spin control and read-out (purple). **c** Actual pulse scheme as implemented in the simulations as well as expectation values along x, y, z for each spin involved in case of $\phi = \pi$. The top panel shows the implemented pulse scheme where X and Y represent the rotation axes and the subscript indicates the rotation angle. The next two panels show the time-evolution of spins A and B under driving, followed by the

concurrence C which serves as direct measure of entanglement in the simulation. The last panel shows the time evolution of the sensor spin when reading out spin A as well as the corresponding time-averaged entanglement witness $\mathcal{W}_R(t_{\text{meas}})$. The entanglement witness reaches the steady state within the first ≈ 40 ns of the measurement time. Idealized parameters were used for clarity: $T = 10$ mK, $\Omega = 0.04$ GHz, $T_1^R = 20$ ns, no relaxation for A and B, and Larmor frequencies and exchange couplings are in GHz as indicated in (a).

confirmed that this maximizes the read-out of the sensor spin in our scheme and does not influence the outcome of the entanglement.

We drive all spins on resonance using a control field of the form $\Omega \cos(\omega_{RF}t + \phi)\hat{\sigma}_x$, with Ω the Rabi rate, ω_{RF} the angular radio-frequency resonant with a desired transition, ϕ an adjustable phase and $\hat{\sigma}_x$ the Pauli matrix. It was previously shown that this approach leads to efficient ESR in excellent agreement with the experiment⁶. For disentanglement we use the same gate sequence but in opposite order while matching the initial phase of each subsequent pulse to the phase of the previous pulse. The upper 3 panels of Fig. 2c show the expectation values for the spin operator $\langle S \rangle$ under these driving fields. We note that the appearance of filled areas is due to crosstalk of the driving frequencies of the pulses and the very fast Larmor precession (10–20 GHz) of each individual spin (see inset), due to the choice that we implemented the simulation in a lab frame of reference. ϕ of the second CNOT was chosen to be π , so that it mimics half a free evolution in the entangled state resulting in a spin flip of A at the end of the scheme whereas spin B remains unchanged. At the point where the spin should be entangled the expectation value of $\langle S_z \rangle$ for A and B are 0, indicating that the spins lie at the equator of their Bloch spheres. To further confirm entanglement we also plot the concurrence C , which is bounded between 0 for non-entangled and 1 for maximally entangled states²⁰. For a bipartite qubit density matrix ρ_{AB} , C is straightforward to calculate and at the point of entanglement the concurrence approaches 1 for the chosen parameter set.

Read-out of the final target spin states is achieved by a long RF pulse on R conditioned on the spin state to be read out. In this part of the sequence quantum properties like the phase of the pulse play a lesser role, as the coherence of spin R is known to be limited by the conduction electrons⁶. Figure 2b shows the transition that is driven for read-out of spin A. In the ESR-STM experiment a long DC voltage pulse could be used to measure the resulting oscillation as a change in the tunneling current ΔI^{ESR} . We set a fast decay time ($T_1 = 20$ ns) for R mimicking this DC pulse and make sure the measurement pulse is relatively long ($t_{\text{meas}} = 100$ ns) such that R quickly reaches the steady state and the signal becomes only dependent on the spin which is read out. Note that we consider this relaxation only during the read-out since for the other parts of the scheme the DC pulse would not be

present. The bottom panel of Fig. 2c shows the evolution of the sensor spin during read-out of spin A. The oscillation of A as a function of ϕ serves as a witness of entanglement and in Fig. 2c $\phi = \pi$ so that this oscillation is at its maximum. We refer to the maximum variation of the sensor spin as the measurement contrast \mathcal{W}_R . Due to the nature of the steady state it is at most half the amplitude of $\langle S_z \rangle$ of A. We see that in the present case the integrated signal of $\langle S_z \rangle$ of R approaches 0.5 within the measurement time. This shows that when the concurrence is 1 the read-out scheme gives the correct output for \mathcal{W}_R . A detailed discussion of the direct relation between \mathcal{W}_R and C can be found in supplementary information I.

The results in Fig. 3 demonstrate the concept in two ways: Fig. 3a shows the entire entanglement protocol while Fig. 3b contrasts the results for non-entangled spins. We will first consider results without any relaxation of spins A and B and at a very low temperature of 10 mK. Larmor frequencies, exchange couplings, and Rabi rates must be chosen such that we stay in the weakly coupled regime while limiting crosstalk, i.e. unwanted driving of other transitions depending on the realistic resonance line widths in the experiment. In addition, we want the Larmor frequencies to be as high as possible to ensure most of the population is in the ground state. Here, we limited the frequency range to 10 – 20 GHz which is routinely achieved for single Ti spins on MgO surfaces ($S = 1/2$) in ESR-STM setups^{4,21,22}. The system parameters are the same as in Fig. 2a. In Fig. 3c–f we show two resulting quantities: first, the variation of each target spin as directly obtained from the density matrix, which is evidence of the entanglement but is not accessible with the ESR-STM. Second, we show the expected read-out signal \mathcal{W}_R , which is a direct observable of the experiment since for the sensor spin $\langle S_z \rangle \propto \Delta I^{\text{ESR}}$. Contrasting both shows that while \mathcal{W}_R is reduced, clearly the signal on the sensor spin directly reflects the spin dynamics in the measurement scheme. We note that in this scheme the phase of the second Hadamard is swept by the equal amount of the free time-evolution, such that $\phi = \omega\tau$, where ω is the angular frequency associated with the entangled state. While the pulse sequence in Fig. 3a can be directly implemented, a real ESR-STM measurement also requires an empty cycle (B-cycle), which can be implemented as shown in Fig. 3b. In this cycle, the background current of the experiment can be measured by simply not entangling the states, which

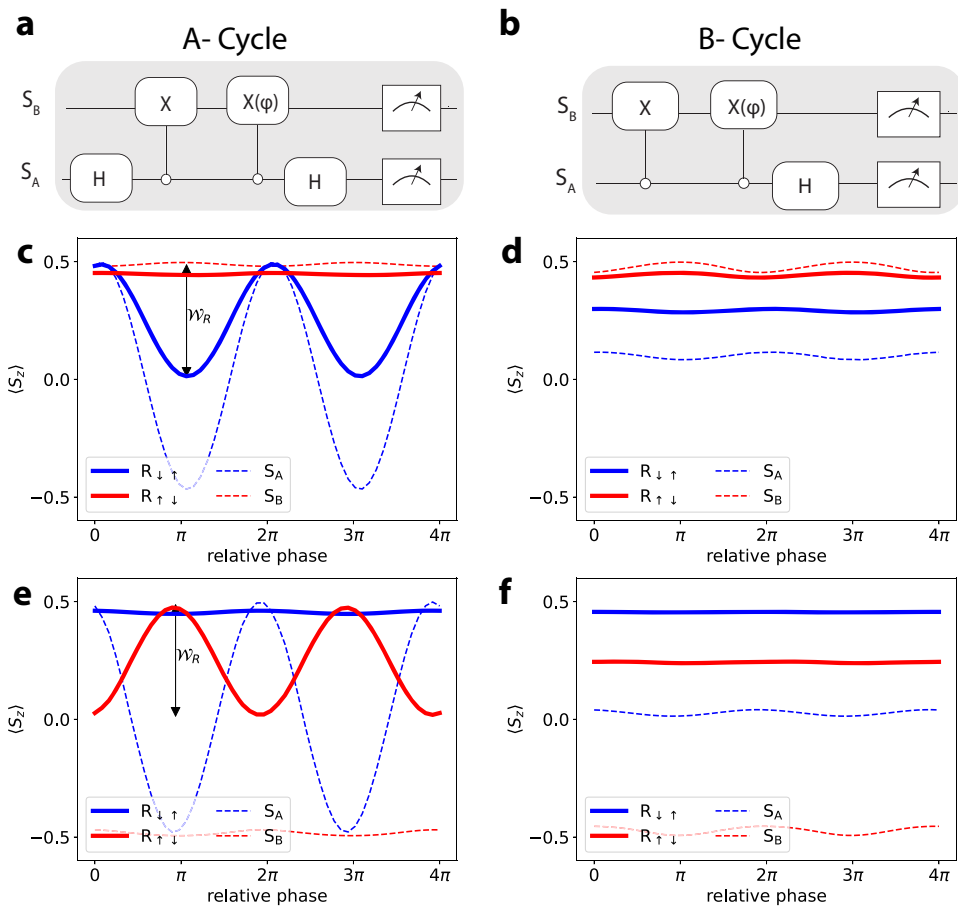


Fig. 3 | Simulations of two-qubit entanglement in ESR-STM showing expected measurement outcomes, where we compare the expectation values $\langle S_z \rangle$ of each spin (inaccessible in the experiment) as well as the indirect read-out \mathcal{W}_R of these values through the sensor spin. From top to bottom (a, c, e) we compare the entangled subspace for different initial states ($|\uparrow\uparrow\rangle, |\downarrow\downarrow\rangle, |\uparrow\downarrow\rangle$). The (b, d, f) on the right

side shows simulations for the same system but for not entangled states (achieved by removing the Hadamard gate), which could serve as empty cycle for the lock-in detection in the ESR-STM experiment. The system parameters are as shown in Fig. 2a, $T = 10$ mK, no relaxation for spins A, B, and $T_1 = 20$ ns for the sensor spin during read-out.

is achieved by removing the Hadamard gate during the entanglement step. We note that the choice of the B-cycle gate sequence is not unique and several different B-cycles are used in ESR-STM experiments (see also supplementary information VI). Finally, in Fig. 3e we show that the method is not limited to the ($|\downarrow\downarrow\rangle, |\uparrow\uparrow\rangle$) subspace. Here, we initialize the system in $|\uparrow\downarrow\rangle$ such that the H and CNOT gate bring the overall target state to $|\uparrow\uparrow\rangle + |\downarrow\downarrow\rangle$. Note that here we drive $|\uparrow\downarrow\rangle$ to $|\downarrow\downarrow\rangle$ for H. The major difference in Fig. 3e when compared to Fig. 3c is that now the oscillation appears in the read-out of $|\downarrow_A \downarrow_B\rangle$ instead of $|\downarrow_A \uparrow_B\rangle$. This in turn allows to identify all the different Bell states in this system.

Discussion

We now turn to the effect of finite lifetime T_1 and elevated temperatures relevant to typical ESR-STM experiments. Previous works have shown that the coherence of Ti spins on two monolayers of MgO on Ag is lifetime limited such that $T_2 = 2T_1$, which allows us to discuss the first results without considering additional pure dephasing^{6,9,18}. As can be seen in Fig. 4a the T_2 time of the two entangled spins (taken here to be identical) has a rather modest influence in the experimentally relevant range of $T_2 > 300$ ns. This is illustrated as well by Fig. 4b, which shows a slice at $T = 0.1$ K. Such low temperatures are typically achieved by using a dilution refrigerator equipped ESR-STM which can reach base-temperatures close to 20 mK^{23,24}. Clearly, in all cases a T_2 of around 300 ns allows for efficient entanglement detection. Temperature is a more critical parameter since the system is initialized purely by temperature. Temperatures that are high compared to the energy splitting of the eigenstates cause excited energy states to be populated. The

effect of this is twofold: i) the system is not fully initialized to the ground state which reduces \mathcal{C} and \mathcal{W}_R , ii) parts of the population that are in excited states additionally reduce \mathcal{C} , but do not participate in \mathcal{W}_R . Though this effect is in general small at elevated temperatures it is non-negligible. This becomes apparent in Fig. 4c where we show another slice of Fig. 4a but now for $T_2 = 300$ ns. Above 300 mK the concurrence as well as \mathcal{W}_R drastically drop and the concurrences reaches 0 at 700 mK. At the same time, \mathcal{W}_R seems to have a non-zero value, indicating entanglement in a not-entangled system. For \mathcal{W}_R to stay an appropriate witness of entanglement we need to subtract an offset with upper bound $O = \sqrt{p_{\uparrow\uparrow\downarrow} p_{\downarrow\uparrow\uparrow}}$ where p are the eigenstate populations in thermal equilibrium (see supplementary information IV). This offset upper bound can be calculated straightforwardly from the initial populations and is defined such that $\mathcal{W}_R - O$ cannot be negative, resulting in a reliable witness of entanglement for all temperatures. This is why for all simulations, including Fig. 4a, b we report $\mathcal{W}_R - O$.

The same physical principles apply to all systems purely initialized by temperature. To avoid these limitations, alternative systems where the initialization is achieved by e.g. pumping and independent of system temperature should be used.

We now investigate the relation between \mathcal{C} and $\mathcal{W}_R - O$ in Fig. 4d where we plot $\mathcal{W}_R - O$ against \mathcal{C} for T sweeps at various T_2 . The underlying relation is linear as in the ideal zero temperature limit (see supplementary information I, III and V). The solid lines in Fig. 4d are the linear dependencies that best match the data (details are in Table 1). The dashed line is the analytic solution in the limit of infinite T_2 (see supplementary information III). Finally, in Fig. 4e we plot $\mathcal{W}_R - O$ against \mathcal{C} for T_2 sweeps at

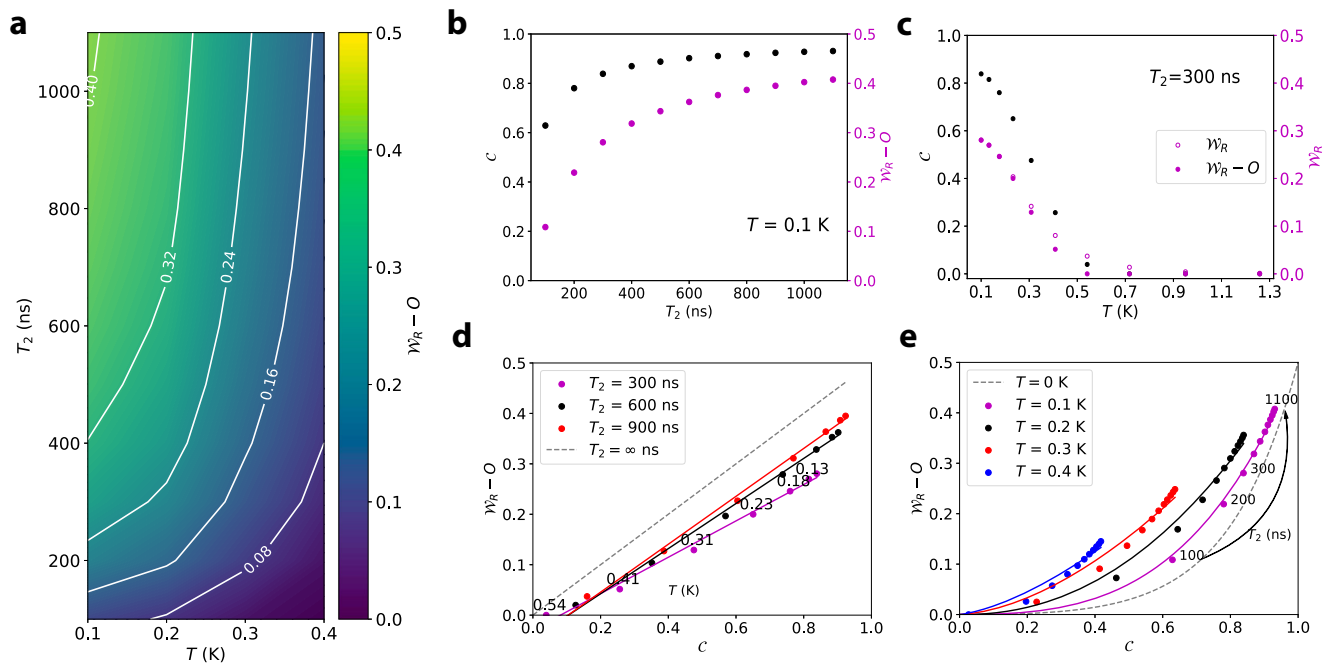


Fig. 4 | Influence of finite lifetime and temperature on the entanglement. **a** shows $\mathcal{W}_R - O$ as function of temperature and decoherence time T_2 (where $T_2 = 2 \cdot T_1$). **(b)** slice of **(a)** showing $\mathcal{W}_R - O$ together with the concurrence C for $T = 0.1$ K as achievable by dilution refrigerators. **(c)** slice of **(a)** showing $\mathcal{W}_R - O$ together with C for $T_2 = 300$ ns. Clearly, temperature is a critical factor and the concurrence drops drastically above 0.3 K. We also plot \mathcal{W}_R such that the difference of subtracting O

becomes apparent. **d** Relation of C and $\mathcal{W}_R - O$ for three different T_2 . Solid lines are linear fits. The dashed line represents the analytical limit for $T_2 \rightarrow \infty$ **(e)** relation of C and $\mathcal{W}_R - O$ for four different temperatures. Solid lines are logarithmic weighted power law fits. The dashed line represents the analytical limit for $T \rightarrow 0$ The system parameters are as shown in Fig. 2a.

Table 1 | Fitting results of $\mathcal{W}_R - O = a + bC$, for the data shown in Fig. 4e

T_2 (ns)	a	b
300	0.36 ± 0.03	-0.03 ± 0.02
600	0.44 ± 0.02	-0.05 ± 0.02
900	0.47 ± 0.02	-0.05 ± 0.02

Uncertainties represent the 2σ confidence interval.

Table 2 | Fitting results of $\mathcal{W}_R - O = \frac{C^2}{2a \ln C} (C^a - 1)$, for the data shown in Fig. 4e

T (K)	a
0.1	2.43 ± 0.23
0.2	0.43 ± 0.24
0.3	-0.60 ± 0.15
0.4	-0.90 ± 0.10

Uncertainties represent the 2σ confidence interval.

various temperatures. We see here that the dependence can best be fitted with a logarithmic scaled power law, which reflects that for lower T_2 there is more decay of the read-out than of the concurrence (see supplementary information II and V). Solid lines in Fig. 4e represent fits of the form $\mathcal{W}_R - O = \frac{C^2}{2a \ln C} (C^a - 1)$ (details are in Table 2). The dashed line is the analytic solution in the limit of zero T (see supplementary information II). Deviations from the fits can be attributed to missing terms in O (see

supplementary information IV), additional remaining cross-talk in the driving pulse scheme and exchange mixing between spin eigenstates causing a more complicated relation between driving strengths and Rabi times.

Finally, we address the influence of noise on the entanglement detection. First, we consider the influence of quantum noise causing pure dephasing, such that the coherence time is no longer lifetime limited but reduced by additional processes leading to an effective coherence time of $1/T_2^* = 1/T_2 + 1/T_\phi$. T_ϕ is the time constant of the pure dephasing process. In the following, $T_2 = 2T_1 = 300$ ns as typical for the experiments⁹. As shown in Fig. 5a and b, even fast dephasing processes with a dephasing time around $T_2^* = 75$ ns still allow for sufficient concurrence and $\mathcal{W}_R - O$. It is not surprising that longer T_2^* times are desirable as this is generally the case in quantum coherent systems, but it is encouraging that in the typical experimental range of $T_2^* \approx 300$ ns^{6,9,18} concurrence and $\mathcal{W}_R - O$ are still relatively high. Second, we consider the influence of classical noise. Experiments have indicated that despite the excellent mechanical stability of STM systems, slow variation of the tip height can occur during the measurement. In our setup, such a variation would change the local magnetic field of the sensor and thereby the resonance frequency f_0 of the sensor^{6,25}. We employ a simple noise model by imposing a Gaussian distribution ($\mu = f_0$, $\sigma = 30$ MHz) on the sensor and perform 100 calculations. We analyzed the resulting variation of $\mathcal{W}_R - O$ shown in Fig. 5c for three representative cases: The best case scenario ($T = 0.01$ K, $T_2 = \infty$ for the target spins) gives the highest contrast and detection should be easy and reliable. In the intermediate case ($T = 0.1$ K, $T_2 = 300$ ns) $\mathcal{W}_R - O$ is narrowly peaked around 0.28, which should still give a very reliable read-out. In the case of high temperature and short T_2 ($T = 0.4$ K, $T_2 = 300$ ns) $\mathcal{W}_R - O$ is small (≈ 0.045), it is, however, still very narrowly distributed which indicates that with appropriate care in the measurement this could still be measurable.

Summarizing, we have shown by open quantum systems simulations that two exchange coupled and relatively long-lived spins can be

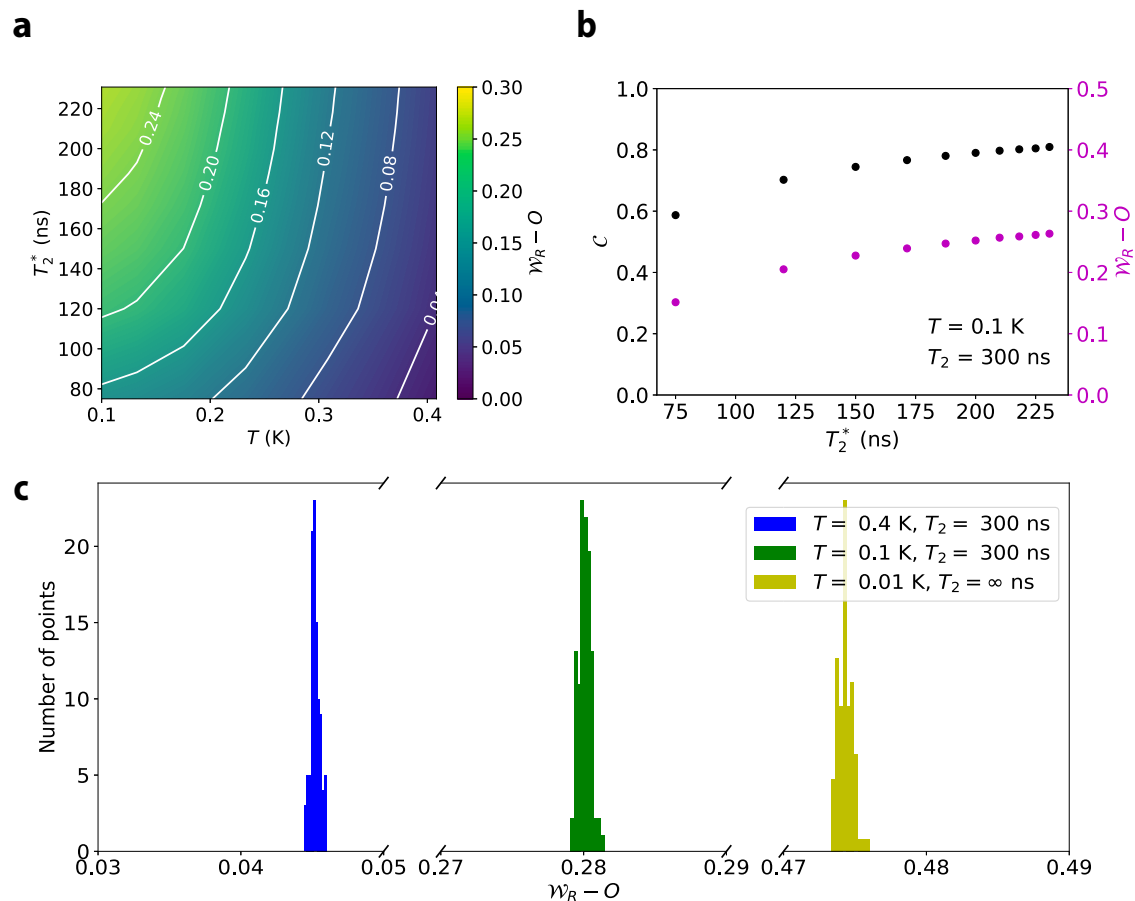


Fig. 5 | Influence of noise on the entanglement. **a** shows the achievable concurrence and read-out contrast $\mathcal{W}_R - O$ as function of pure dephasing time T_2^* . **b** shows C and $\mathcal{W}_R - O$ as function of T_2^* for a fixed $T_2 = 300$ ns for the two spins and $T = 0.1$ K. **c** $\mathcal{W}_R - O$ as function of Gaussian magnetic field noise causing fluctuations of the resonance frequency of the sensor spin with $\sigma = 30$ MHz for three representative cases characterized by T and T_2 .

entangled and that the entanglement can be directly measured by ESR-STM using a third, weakly coupled sensor spin. Our simulations indicate that temperature is critical to achieve high degree of entanglement and \mathcal{W}_R , due to the fact that the populations are initialized into thermal equilibrium. Systems that can be initialized more independently from temperature as usually done in optical qubits in trapped ion systems for example, could overcome the strict temperature requirement. For physical spins on surface systems available today, such as the widely studied Ti on MgO/Ag(001), entanglement should be achievable and in principle measurable with $T_2 = 300$ ns for the quantum spins and $T_1 \approx 20$ ns for the sensor spin at temperatures up to 400 mK. High degrees of entanglement $C \approx 0.8$ and corresponding read-out can be reached when using a dilution refrigerator at $T \approx 100$ mK.

Methods

All calculations were performed using a converged time step depending on the pulse scheme but such that it was always smaller than 8 ps. Following previous works⁶, we modeled each spin as a Zeeman energy term $2\pi f_{L,i} S_{z,i}$ with $f_{L,i}$ the i -th Larmor frequency, and pairwise isotropic exchange coupling terms $J_{ij} \vec{S}_i \cdot \vec{S}_j$. ESR driving is achieved by applying the necessary single-frequency driving terms $\Omega_k \cos(\omega_k(t - t_k^{\text{start}}) + \phi_k) \sigma_{x,i}(t_k^{\text{start}} < t < t_k^{\text{end}})$, with ω_k the frequency of the pulse matching the desired energy transition, t_k^{start} and t_k^{end} the start and end times of the pulse and ϕ_k is an adjustable phase. Ω_k is the on-resonance Rabi rate, $k = 1 \dots N$ the index of driving frequency terms. The maximum number of driving terms in our simulation was $N \leq 7$. The total system Hamiltonian can be written as follows:

System Hamiltonian:

$$H_{\text{tot}} = \sum_{i=1}^3 2\pi f_{L,i} S_{z,i} + \sum_{i=1}^3 \sum_{j>i}^3 J_{ij} \vec{S}_i \cdot \vec{S}_j + \sum_k \sum_{i=1}^3 \Omega_k \times \cos(\omega_k(t - t_k^{\text{start}}) + \phi_k) \sigma_{x,i}(t_k^{\text{start}} < t < t_k^{\text{end}}) \quad (1)$$

Lindblad equation: We solved a Lindblad equation for the reduced density matrix ρ of the following form

$$\frac{d\rho}{dt} = -\frac{i}{\hbar} [H_{\text{tot}}, \rho] + \sum_l \left(\mathcal{L}_l \rho \mathcal{L}_l^\dagger - \frac{1}{2} \mathcal{L}_l^\dagger \mathcal{L}_l \rho - \frac{1}{2} \rho \mathcal{L}_l^\dagger \mathcal{L}_l \right) \quad (2)$$

The last term on the right-hand side are the collapse operators for our system. We used two sets of collapse operators $\mathcal{L}^{\text{Kondo}} + \mathcal{L}^\phi$ to model spin energy relaxation as well as pure dephasing.

Collapse operators: The first set of collapse operators was defined acting on the coupled three-spin system in order to model Kondo spin relaxation, known to be the main source of decoherence for these systems^{4,26,27}. We arrive at these terms by writing the known rate equation (see for example Eq. (4) of supplementary of ref. 28) in Lindblad form. The operator acting between energy level m and n of the system is

$$\mathcal{L}_{m,n}^{\text{Kondo}} = \sqrt{\sum_l |J_l \sum_{s_i, s_j} \langle m, s_i | \vec{s}_i \otimes \vec{S}_l | n, s_j \rangle|^2 \frac{\epsilon_{mn}}{e^{\epsilon_{mn}/k_B T} - 1}} |m\rangle \langle n|. \quad (3)$$

Here the first sum is over the l different atomic spins and the second sum is over the initial (s_i) and final (s_f) state of the itinerant electron spin interacting with these spins. \vec{S} and \vec{s} are the respective spin operators. ϵ_{mn} is the energy difference between m and n of the three-spin system. Finally, J_l is the strength of the interaction with each atomic spin. In low temperature approximation it relates to the isolated l -th spin relaxation time $T_{1,l}$ and energy of its Larmor frequency ϵ_l as (see Eq. 69 of ref. 27)

$$J_l = \sqrt{\frac{1}{\epsilon_l T_{1,l}}}. \quad (4)$$

The second set of operators is for pure dephasing. Here, the standard operators are used relating the pure dephasing rate to the pure dephasing time $T_{\phi,l}$ via the Pauli- z matrix for the l -th spin, i.e. $\sigma_{z,l} = \mathbb{1} \otimes \dots \otimes \sigma_z \otimes \dots \otimes \mathbb{1}$.

$$\mathcal{L}_l^\phi = \sqrt{\frac{1}{2T_{\phi,l}}} \sigma_{z,l}. \quad (5)$$

Read-out: For read-out long pulses were sent resonant with transitions of S_R . The expectation value of S_R was averaged in 16000 time steps for a time of 100 ns. In order to have a converged expectation value a Rabi strength was used double the other strengths used in the scheme.

Fitting results: The relations between $\mathcal{W}_R - O$ and C in Fig. 4d were fit using $\mathcal{W}_R - O = a + bC$ reflecting the up to first order linear dependence as derived in supplementary information III and IV. The fitting results are reported in Table 1. The relations between \mathcal{W}_R and C in Fig. 4e were best fit using a logarithmic weighted power law function of the form $\mathcal{W}_R - O = \frac{c^2}{2a \ln c} (C^a - 1)$. The fitting results are reported in Table 2. Derivations are in supplementary information II and IV.

Concurrence: For concurrence calculation first the partial trace over S_R was taken leaving the reduced matrix in the target spin basis. Then for each entanglement scheme the maximum was reported.

Data availability

All data generated or analyzed during this study are included in ref. 29.

Code availability

The underlying code for this study is available and can be accessed via³⁰.

Received: 30 January 2024; Accepted: 8 September 2024;

Published online: 28 September 2024

References

- Crommie, M. F., Lutz, C. P. & Eigler, D. M. Confinement of electrons to quantum corrals on a metal surface. *Science* **262**, 218–220 (1993).
- Yang, K. et al. Engineering the eigenstates of coupled spin-1/2 atoms on a surface. *Phys. Rev. Lett.* **119**, 1–8 (2017).
- Baumann, S. et al. Electron paramagnetic resonance of individual atoms on a surface. *Science* **350**, 417–420 (2015).
- Yang, K. et al. Coherent spin manipulation of individual atoms on a surface. *Science* **366**, 509–512 (2019).
- Phark, S. H. et al. Electric-field-driven spin resonance by on-surface exchange coupling to a single-atom magnet. *Adv. Sci.* **10**, 1–8 (2023).
- Phark, S. H. et al. Double-resonance spectroscopy of coupled electron spins on a surface. *ACS Nano* **17**, 14144–14151 (2023).
- Reina-Gálvez, J., Lorente, N., Delgado, F. & Arrachea, L. All-electric electron spin resonance studied by means of Floquet quantum master equations. *Phys. Rev. B* **104**, 1–16 (2021).
- Reina-Gálvez, J., Wolf, C. & Lorente, N. Many-body nonequilibrium effects in all-electric electron spin resonance. *Phys. Rev. B* **107**, 235404 (2023).
- Wang, Y. et al. An atomic-scale multi-qubit platform. *Science* **382**, 87–92 (2023).
- Jozsa, R. & Linden, N. On the role of entanglement in quantum-computational speed-up. *Proc. Roy. Soc. Lond. Ser. A: Math. Phys. Eng. Sci.* **459**, 2011–2032 (2003).
- Rieffel, E. G. & Polak, W. H. *Quantum Computing: A Gentle Introduction* (MIT Press, 2011). <https://books.google.co.kr/books?id=iYX6AQAQBAJ>.
- Bastiaans, K. M. et al. Amplifier for scanning tunneling microscopy at MHz frequencies. *Rev. Sci. Instrum.* **89**, 93709 (2018).
- Willke, P. et al. Coherent spin control of single molecules on a surface. *ACS Nano* **15**, 17959–17965 (2021).
- Del Castillo, Y. & Fernández-Rossier, J. Certifying entanglement of spins on surfaces using ESR-STM. *Phys. Rev. B* **108**, 1–5 (2023).
- Veldman, L. M. et al. Free coherent evolution of a coupled atomic spin system initialized by electron scattering. *Science* **372**, 964–968 (2021).
- Wei, K. X. et al. Verifying multipartite entangled Greenberger-Horne-Zeilinger states via multiple quantum coherences. *Phys. Rev. A* **101**, 1–10 (2020).
- Stemp, H. G. et al. Tomography of entangling two-qubit logic operations in exchange-coupled donor electron spin qubits. Preprint at <http://arxiv.org/abs/2309.15463> (2023).
- Wang, Y. et al. Universal quantum control of an atomic spin qubit on a surface. *npj Quantum Inform.* **9**, 3–8 (2023).
- Johansson, J. R., Nation, P. D. & Nori, F. QuTiP: an open-source Python framework for the dynamics of open quantum systems. *Comput. Phys. Commun.* **183**, 1760–1772 (2012).
- Hill, S. & Wootters, W. K. Entanglement of a pair of quantum bits. *Phys. Rev. Lett.* **78**, 5022–5025 (1997).
- Reale, S. et al. Electrically driven spin resonance of 4f electrons in a single atom on a surface. *Nat. Commun.* **15**, 5289, (2024)
- Seifert, T. S. et al. Single-atom electron paramagnetic resonance in a scanning tunneling microscope driven by a radio-frequency antenna at 4 K. *Phys. Rev. Res.* **2**, 013032 (2020).
- Kim, J. et al. Spin resonance amplitude and frequency of a single atom on a surface in a vector magnetic field. *Phys. Rev. B* **104**, 174408 (2021).
- van Weerdenburg, W. M. J. et al. A scanning tunneling microscope capable of electron spin resonance and pump-probe spectroscopy at mK temperature and in vector magnetic field. *Rev. Sci. Instrum.* **92**, 033906 (2021).
- Willke, P. et al. Probing quantum coherence in single-atom electron spin resonance. *Sci. Adv.* **4**, eaaq1543 (2018).
- Ternes, M. Spin excitations and correlations in scanning tunneling spectroscopy. *N. J. Phys.* **17**, 63016 (2015).
- Delgado, F. & Fernández-Rossier, J. Spin decoherence of magnetic atoms on surfaces. *Prog. Surf. Sci.* **92**, 40–82 (2017).
- Loth, S., Lutz, C. P. & Heinrich, A. J. Spin-polarized spin excitation spectroscopy. *N. J. Phys.* **12**, 125021 (2010).
- Broekhoven, R., Lee, C., Phark, S.-h., Otte, S. & Wolf, C. Protocol for certifying entanglement in surface spin systems using a scanning tunneling microscope. <https://doi.org/10.5281/zenodo.10530510> (2024).
- Broekhoven, R., Wolf, C. & Lee, C. Module to model pulsed esr in stm experiments. <https://doi.org/10.5281/zenodo.10528113> (2024).

Acknowledgements

The authors thank N. Lorente for his insight related to entanglement in surface spin systems. Further we thank G. Giedke, F. Donati and H. Stemp for discussions. This work was supported by the Institute for Basic Science (IBS-R027-D1). R. B. and S. O. acknowledge support from the Netherlands Organisation for Scientific Research (NWO Vici Grant VI.C.182.016).

Author contributions

RB, SP, and CW conceived the paper, RB and CL performed numerical simulations, all authors contributed to the discussion and the writing of the manuscript.

Competing interests

The authors declare no competing interests.

Additional information

Supplementary information The online version contains supplementary material available at <https://doi.org/10.1038/s41534-024-00888-9>.

Correspondence and requests for materials should be addressed to Christoph Wolf.

Reprints and permissions information is available at <http://www.nature.com/reprints>

Publisher's note Springer Nature remains neutral with regard to jurisdictional claims in published maps and institutional affiliations.

Open Access This article is licensed under a Creative Commons Attribution 4.0 International License, which permits use, sharing, adaptation, distribution and reproduction in any medium or format, as long as you give appropriate credit to the original author(s) and the source, provide a link to the Creative Commons licence, and indicate if changes were made. The images or other third party material in this article are included in the article's Creative Commons licence, unless indicated otherwise in a credit line to the material. If material is not included in the article's Creative Commons licence and your intended use is not permitted by statutory regulation or exceeds the permitted use, you will need to obtain permission directly from the copyright holder. To view a copy of this licence, visit <http://creativecommons.org/licenses/by/4.0/>.

© The Author(s) 2024